Decrypting the Non-Adiabatic Photoinduced Electron Transfer Mechanism in Light-Sensing Cryptochrome

Gustavo J. Costa and Ruibin Liang*

Department of Chemistry and Biochemistry, Texas Tech University, Lubbock, TX, 79409, USA

AUTHOR INFORMATION

Corresponding Author

*Ruibin Liang

Email address: rliang@ttu.edu

Abstract

Cryptochromes are blue light photoreceptors found in organisms from plants to animals, playing various critical roles in life processes such as circadian rhythms, phototropism and magnetoreception. In light-sensing cryptochromes, the photoexcitation of the flavin adenine dinucleotide (FAD) cofactor triggers a cascade of electron transfer events via a tryptophan chain, eventually generating a radical pair crucial for signaling. Despite extensive studies, the initial photoinduced electron transfer (ET) from a neighboring tryptophan residue to FAD remains unclear due to the complexity of simulating all-atom dynamics in excited states, particularly regarding the roles of non-adiabatic pathways and protein environment on the reaction kinetics and quantum efficiency of the ET. To address this gap, we performed extensive non-adiabatic and adiabatic dynamics simulations with on-the-fly multireference *ab initio* electronic structure calculations of *Arabidopsis thaliana* cryptochrome 1 (*At*CRY1). Our results reveal a novel photoinduced electron transfer mechanism involving non-radiative decay from higher-lying singlet states, which proceeds much faster than the adiabatic electron transfer on the S_1 state. The adiabatic process is hindered by a newly discovered low-energy S_1 local excitation minimum. In contrast, non-adiabatic relaxation can rapidly reach a dynamically stable S_1 charge-transfer minimum, setting the stage for subsequent electron transfer steps. Additionally, the protein environment stabilizes the orientation of tryptophan residues, facilitating later ET events between them while hindering the initial FAD-W400 transfer. These new insights greatly enhance our fundamental understanding of photoinduced electron transfer in cryptochromes and the structure-function relationships in photoreceptors in general.

Keywords: photobiology, cryptochromes, non-adiabatic dynamics, QM/MM simulation, multireference electronic structure methods

Introduction

Cryptochromes are blue-light photoreceptors in plants and animals[1-10]. They play essential roles in many biological processes, such as circadian rhythms[2, 5, 11-13], photomorphogenesis, and phototropism in plants[1, 3, 14, 15], and the sensing of magnetic fields in migratory animals.[16-19] Light-sensing cryptochromes bind the flavin adenine dinucleotide (FAD)[20] as the cofactor, which absorbs blue light and induce long-range electron transfer (ET) processes across a chain of tryptophan residues. In its dark-adapted state, the isoalloxazine ring of FAD is fully oxidized.[21, 22] After the FAD is photoexcited, the nearest tryptophan residue donates an electron to the isoalloxazine ring of FAD. The rate of this first photoinduced ET step depends on the type of cryptochrome, ranging from ~1 ps in animal cryptochromes such as CRY4[21, 23, 24] and sub-picosecond timescale in plant cryptochromes such as *At*CRY1.[19, 25] The subsequent ET steps through the chain of tryptophan residues eventually create a coupled radical pair separated by a long distance (>15 Å). This radical pair creates the signaling state of the cryptochrome.

A comprehensive understanding of the initial ET from the closest trptophan residue to the FAD is essential for elucidating how the radical pair is created and propagated to create the signaling state of cryptochromes. Despite numerous previous studies[6, 19, 26-36], fundamental mechanistic questions remain unresolved regarding this essential ET step. For example, does the ET occur adiabatically on a single excited state, or does it involve non-adiabatic relaxation from higher-lying electronic states? What is the role of the protein environment in ET kinetics? Addressing these fundamental questions could offer a valuable perspective for interpreting time-resolved spectroscopy experiments[25, 37] and advancing the field of photobiology in general. Simulations that quantify the thermodynamics and dynamics of ET are necessary for answering these questions. Previous studies on cryptochromes using well-established ET models such as Marcus theory[26, 28, 38-40] and optimized excited-states structures[41] are undoubtedly successful at understanding the ET mechanism in cryptochromes, but they also have limitations. For

example, the assumption of equilibrium statistical mechanics is often questionable in the regime of ultrafast ET in biomolecules where nonergodic effects are prominent[42-46], such as in the case of cryptochromes. Moreover, these models lack the atomic-level details of real-time ET dynamics in proteins. In this regard, all-atom dynamics simulations are indispensable to complement traditional ET models because they directly propagate the coupled motions of nuclei and electrons without introducing assumptions such as ergodicity and (non)adiabaticity[38-40].

However, it is very challenging to perform all-atom direct dynamics simulations of the ET process in the excited-states manifold of proteins. This is mainly due to the high cost of dynamics simulations with on-the-fly potential energy surface (PES) evaluations using accurate excited-state electronic structure methods. It is even more challenging to accurately simulate the non-adiabatic ET events involving transitions among multiple adiabatic electronic states, which necessitate the correct treatment of the coupled motions of the electronic and nuclear degrees of freedom of the biomolecular system. Although a coarse-grained semi-empirical method has been applied to model the ET dynamics in cryptochrome[27, 30, 47], these studies were not focused on the first ET step from TRP to FAD, and the accuracy of the semi-empirical method may need further improvements for non-adiabatic ET processes involving multiple excited states on the FAD.

To address the above-mentioned challenges, in this work, we extensively characterize the first step of the photoinduced ET mechanism in *Arabidopsis thaliana* cryptochrome 1 (*At*CRY1), employing non-adiabatic and adiabatic dynamics simulations in the quantum mechanics/molecular mechanics (QM/MM) setting, with on-the-fly multireference *ab initio* electronic structure calculations. Due to its structural availability, the *At*CRY1 has long served as a model system for studying the functional mechanism of

cryptochromes[26, 48]. Our non-adiabatic dynamics simulations employed the *ab initio* multiple spawning (AIMS) algorithm[49-52] to efficiently and accurately propagate the coupled nuclear and electronic wavefunctions among the excited-state manifold according to the time-dependent Schrödinger's equations. Extensive multi-reference electronic structure calculations were performed: the Complete-Active Space Self-Consistent Field (CASSCF)[53] method was employed in the AIMS simulation and optimizations of critical points and reaction pathways on the excited states. The Extended Multistate Complete Active Space Second-Order Perturbation Theory (XMS-CASPT2)[54], a highly accurate multi-reference *ab initio* method incorporating both static and dynamic electron correlation, was employed to characterize the energies, characters and ordering of excited states at the Franck-Condon (FC) region. The results were further corroborated by extensive excited-state QM/MM adiabatic dynamics simulations using the CASSCF method. The combination of these state-of-the-art simulation methods leads to several major new findings: (1) the non-adiabatic ET is a viable pathway to induce the ultrafast ET between FAD and W400, leading to a stable S_1-state minimum with charge transfer (CT) character, (2) there are two distinct S_1-state minima of local excitation (LE) character, the lower of which slows down the adiabatic ET dynamics, and (3) the protein facilitates the subsequent ET steps among tryptophan residues by stabilizing their side chains, at the cost of slowing down the first ET step between FAD and the W400 residue.

The discussion is organized as follows: (1) characters and ordering of excited states in the FC region; (2) non-adiabatic ET induced by $S_2 \rightarrow S_1$ non-radiative decay, and the discovery and characterization of the S_1-state LE and CT minima; (3) adiabatic ET on the S_1 state following photoexcitation in the FC region, and (4) the role of the protein environment in the ET kinetics.

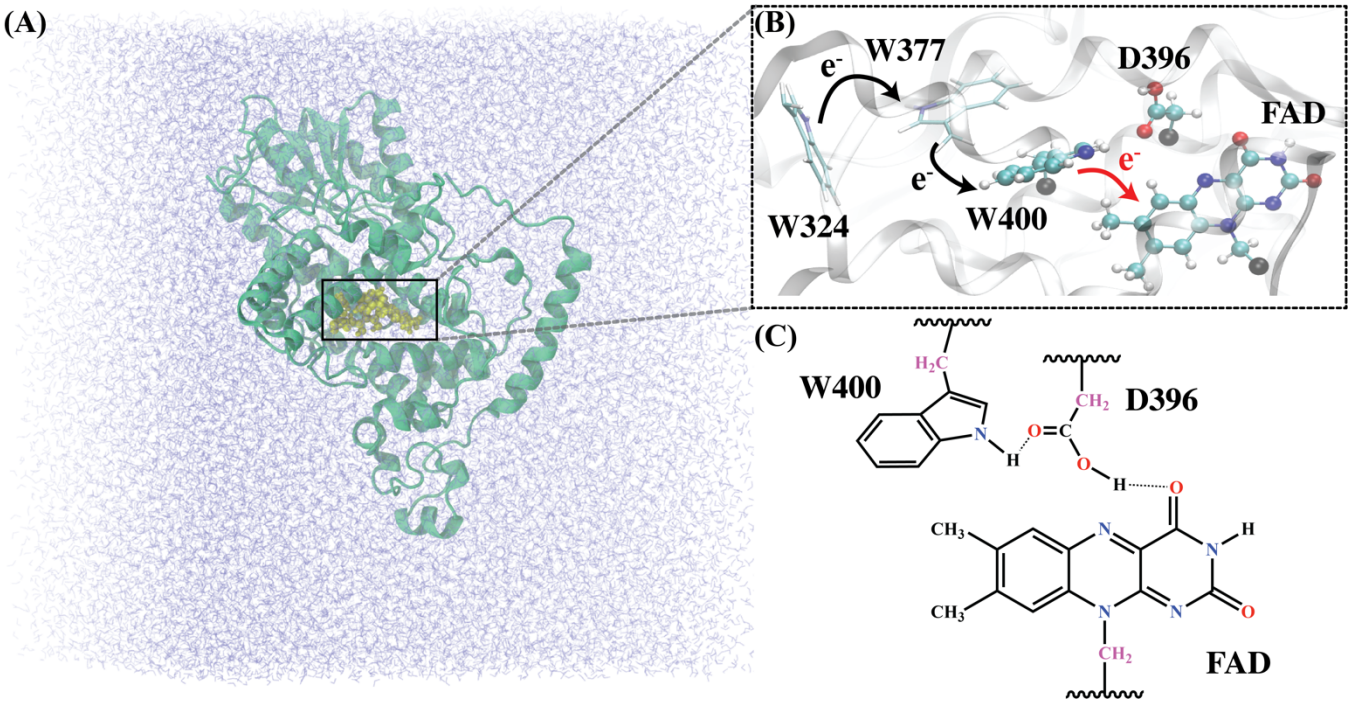

Figure 1. (A) Overview of the simulation box of classical MD simulations, illustrating the *At*CRY1 protein (green) solvated in water (blue). The protein backbone is shown in a ribbon representation, and the ET complex, consisting of the isoalloxazine ring of FAD, the W400, and the protonated D396 residues, is depicted in yellow. (B) The chain of tryptophan residues (W400, W377, W324) and the FAD molecule participating in the cascade of ET events in *At*CRY1. The QM region (W400, D396 and isoalloxazine ring of FAD, i.e., the "FWD" complex), which is essential for describing the initial photoinduced ET (red arrow), is depicted in a ball-and-stick representation. (C) Chemical structures of the QM region. Carbon and hydrogen atoms are shown in black, oxygen in red, and nitrogen in blue. The QM carbon atoms at the QM/MM covalent boundaries are shown in purple.

Results

Low-lying singlet excited states in the Franck-Condon region

After photoexcitation of FAD, an electron is transferred from the W400 residue to FAD (**Fig. 1**). This reaction occurs on the excited state of the FAD-W400 dimer. The photoexcitation initiates a $\pi \rightarrow \pi^*$ transition localized on the fully oxidized FAD, i.e., [FAD*-W400]. The excited-state electronic wavefunction of the FAD-W400 complex is thus dominated by an intramolecular local excitation at the FAD moiety, referred to as "LE character" below. After the ET finishes, a radical pair is formed, i.e., [$FAD^{\bullet+}$-$W400^{\bullet-}$], and the excited-state wavefunction is dominated by an intermolecular charge-transfer

excitation, referred to as "CT character" below. Considering that the FAD forms hydrogen bonds with the W400 and the protonated D396 residues[26, 41] (**Fig. 1C**), together they are referred to as the "FWD complex" below. The FWD complex was treated in the QM region in all QM/MM simulations.

Since the energetics, characters, and ordering of the low-lying singlet states (S_1-S_3) can play a crucial role in the light absorption and subsequent ET dynamics, it is critical to examine them at the Frack-Condon (FC) region. We employed classical MD, ground-state QM/MM MD simulations for ground-state conformational sampling at the FC region, followed by multireference *ab initio* calculations using the XMS-CASPT2 method to characterize the excited states. This multiscale approach included the effects of the environment and the electron correlation on the excited-state properties, which are essential for accurately calculating the absorption spectra (**Fig. 2**).

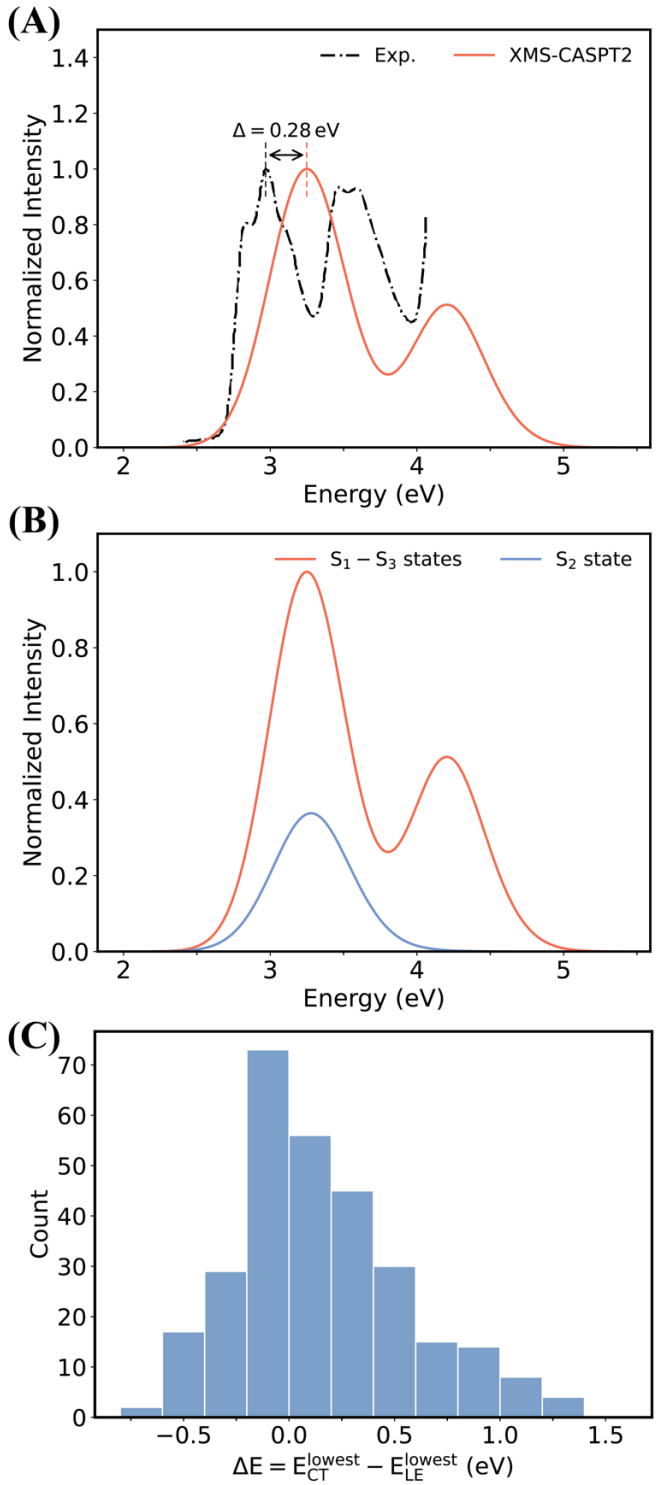

Figure 2. Absorption spectra and excited-state order of the FWD complex in the *At*CRY1 calculated at the XMS-CASPT2//SA-4-CASSCF(6,6)/6-31G*/MM level of theory and compared with experiment. (A) Comparison between calculated spectrum including all $S_0 \rightarrow S_1$-S_3 transitions averaged over 300 ICs sampled on the ground state in the FC region (red curve) with experimental absorption spectrum[24] (black curve) (B) Comparison between the spectrum derived from a subset of 104 ICs (approximately 35%)

whose S_2 state has LE character and $S_0 \rightarrow S_1$ transition has higher oscillator strength than $S_0 \rightarrow S_1$ (blue curve) and all ICs (red curve). (C) Energy gap distribution between the lowest-lying singlet adiabatic excited states with the CT and LE characters in *At*CRY1, i.e., $\Delta E = E_{CT}^{lowest} - E_{LE}^{lowest}$. The energy gaps were calculated for the 300 ICs in the FC region using the XMS-CASPT2//SA-4-CASSCF(6,6)/6-31G*/MM method. Energy gaps approaching zero correspond to ICs near the conical intersections between the LE and CT adiabatic states, which is critical for mediating non-adiabatic transitions between them. Negative energy gaps indicate the possibility of photoexcitation to bright LE adiabatic states higher than the CT states, potentially inducing non-adiabatic ET events.

The experimental absorption spectrum of FAD in *At*CRY1 (**Fig. 2A**, black curve) exhibits two prominent peaks in the range of 2.5 to 4 eV[21, 23, 24]. The maximum absorption wavelength was attributed to local $\pi \rightarrow \pi^*$ electronic transitions at ~2.97 eV. Our QM/MM vertical excitation calculations at the XMS-CASPT2//SA-4-CASSCF(6,6)/6-31G*/MM level of theory reproduced the main spectral features reasonably well, yielding a maximum absorption at 3.25 eV. There is a systematic blue shift of ~0.28 eV compared to the experimental results. This blue shift with respect to the experimental spectra is on par with earlier computational studies[26, 48, 55]. **Fig. S2** illustrates the correlation between the S_0-S_1 energy gap, $S_0 \rightarrow S_1$ oscillator strength (*f*), and S_1-state dipole moment (Debye) for the FDW complex embedded in the AtCRY1. The S_1 states with LE character on the FAD exhibit high oscillator strength and low dipole moments (0–20 Debye), whereas those with CT character involve intermolecular electron transfer from W400 to the FAD moiety, and they exhibit near-zero oscillator strength and high dipole moments (> 25 Debye).

In a previous computational study by Cailliez et al.[26], similar blue shifts in the absorption wavelength with respect to the experiment were observed using TD-DFT with the ωB97X-D functional. Importantly, their calculations predicted that the lowest CT state can have lower energy than the lowest LE state in the FC region. This study[26] thus suggested that singlet states higher than S_1, such as S_2 and S_3, can be initially populated by photoexcitation to initiate ET.

We test this possibility with an accurate multireference *ab initio* method. Specifically, we analyzed the character and ordering of the lowest-lying singlet states calculated by the XMS-CASPT2 method (Method). Approximately 35% of the total 300 sampled ground-state conformations (**Fig. 2B**) feature an S_2 state that is dominated by the LE character and has a larger oscillator strength for $S_0 \rightarrow S_2$ than that of $S_0 \rightarrow S_1$ (see SI Method for the definitions of excited-state characters). Importantly, the excitation energies of these ICs are mostly in the range of the lower energy peak of the spectrum (**Fig. 2B**, blue). This supports the possible scenario that a non-negligible portion of the initial ET originates from photoexciting the FAD to the S_2 state, followed by non-adiabatic relaxation to the S_1 state.

The possibility of this scenario is further corroborated by the distribution of the energy gaps between the lowest-lying adiabatic singlet excited states with dominant CT and LE characters, defined as $\Delta E = E_{CT}^{lowest} - E_{LE}^{lowest}$ (**Fig. 2C**). The fluctuation in the sign of ΔE emphasizes that the order of the lowest excited states with CT and LE characters is sensitive to the ground-state geometry of the FWD complex. The distribution of ΔE features non-negligible frequency at near-zero values, indicating energy degeneracy between the lowest-lying adiabatic states with LE and CT characters. The negative ΔE values indicate a non-negligible probability that the lowest excited state has a CT character and lies below a singlet state with the LE character. Many ICs in this subset have a dominating CT character in the S_1 state. Due to the near-zero $S_0 \rightarrow S_1$ oscillator strength, higher-lying bright singlet states with LE character are more likely to be populated by photoexcitation. Based on these observations, we hypothesize that starting from an S_2 state of LE character, the system may quickly access the S_2/S_1 conical intersection (CI) seam, followed by non-radiative decay to the S_1 state, with some probability of ending up in an S_1 minimum with CT character, completing the first ET step through a non-adiabatic pathway. Below, we explicitly test this hypothesis through non-adiabatic dynamics simulations.

Non-Adiabatic ET through $S_2 \rightarrow S_1$ relaxation

To simulate the initial ET step in *At*CRY1 associated with non-adiabatic $S_2 \rightarrow S_1$ relaxation, the SS-AIMS simulations were initiated from 15 initial conditions (ICs) whose S_2 and S_1 states were dominated by the LE and CT characters, respectively. The SS-AIMS simulations were propagated with on-the-fly QM/MM evaluations of PESs of the S_0-S_3 states using the SA-4-CASSCF(6,6)/6-31G*/MM method. **Fig. 3A** illustrates the time evolutions of the populations of the adiabatic S_1 and S_2 states. It is evident that the $S_2 \rightarrow S_1$ non-radiative decay is ultrafast and mostly completed within 10 fs. The predicted S_2 lifetime is approximately 3.54 ± 0.54 fs within the protein environment. The $S_2 \rightarrow S_1$ decay is mediated by the S_2/S_1 CI seam. The minimal energy conical intersection (MECI) of the S_2 and S_1 states is ~0.2-0.6 eV lower energy than the S_2 state energy on the S_0-state optimized FC points, based on the five ICs we tested. The RMSD between the FC and S_2/S_1 MECI for the FWD complex is small, in the range of 0.06-0.1 Å. Thus, the ultrafast $S_2 \rightarrow S_1$ decay is facilitated by the energetically and geometrically easy access to the S_2/S_1 MECI on the S_2 state from the FC region.

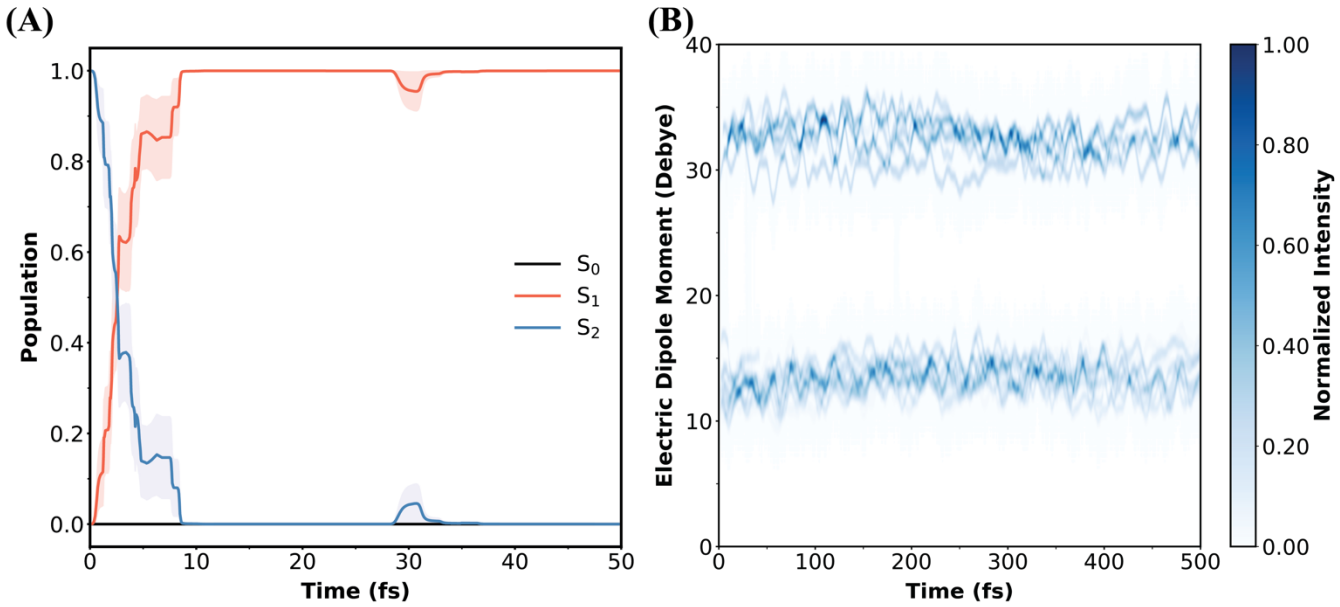

Figure 3. (A) The time evolution of the populations of the S_1 and S_2 excited states in *At*CRY1 following photoexcitation to the S_2 state with bright LE character, extracted from the SS-AIMS non-adiabatic dynamics simulations coupled with the SA-4-CASSCF(6,6)/6-31G*/MM method. The statistical

uncertainties of each curve were computed using the bootstrapping analysis with 1000 samples. (B) The time evolution of the distribution of the excited-state dipole moment (in Debye) in the SS-AIMS non-adiabatic dynamics simulations. The dipole moments were analyzed from all TBFs during the SS-AIMS dynamics. The time-dependent distribution was generated by convolving the dipole moments using fixed-width 2D Gaussians with time-dependent amplitudes of the TBFs (SI method).

To analyze the change in the character of excited-state electronic wavefunctions associated with the $S_2 \rightarrow S_1$ decay, we tracked the distribution of excited-state dipole moments (μ) for the ensemble of TBFs throughout the SS-AIMS simulation. The μ of each TBF residing on each adiabatic state at any given time t was recorded, generating a trajectory of $\mu(t)$ for each TBF. Each $\mu(t)$ was convolved by 2D Gaussians with widths of 1.91 Debye and 0.75 fs, and a time-dependent amplitude that is the same as the TBF. The convolved $\mu(t)$'s were summed up to generate the time-dependent distribution of μ in **Fig. 3B**. This procedure averages over all independent SS-AIMS runs. At any time, electronic wavefunctions with dipole moment less than ~ 20 Debye are assigned as having a dominant LE character, while those above ~ 25 D are assigned as a dominant CT character.

It is evident from **Fig. 3A** that within 10 fs of the SS-AIMS simulation, the TBFs with both LE and CT characters had been spawned onto the S_1 state, and they retained their characters throughout the course of the subsequent adiabatic dynamics on the S_1 state over a few hundreds of femtoseconds. This indicates that the TBFs are dynamically stabilized in the LE and CT minima on the S_1 state. At the end of the SS-AIMS simulation, among the 75 S_1 TBFs, 54 TBFs were classified as LE character and 21 as CT character, leading to a quantum yield of 28% of the non-adiabatic ET event.

It is worth noting that all the 21 S_1 TBFs having a CT character in the S_1 state were generated by non-adiabatic transitions without any contributions from adiabatic transitions following the $S_2 \rightarrow S_1$ decay. Thus, the ~28% quantum yield of ET is solely contributed by $S_2 \rightarrow S_1$ non-radiative decay. This is a significant new finding since it, for the first time, explicitly demonstrates the feasibility of non-adiabatic

ET events in cryptochrome. Non-adiabatic relaxations from higher-lying bright states than S_2 (not simulated here) may further increase the quantum efficiency of ET.

Adiabatic dynamics on S_1 state following $S_2 \rightarrow S_1$ non-radiative decay

The above-mentioned SS-AIMS results not only elucidated the mechanism of the ultrafast non-adiabatic ET step but also revealed the existence of multiple LE and CT minima on the PES of the S_1 state. To characterize these minima, we propagated adiabatic QM/MM trajectories on the S_1 state for another 1 ps in the NVE ensemble to continue the dynamics of SS-AIMS simulations. These trajectories started from the coordinates and velocities of the centroids of all S_1 TBFs that survived at the end of the SS-AIMS simulations. They carried the excess kinetic energy due to non-radiative decay from higher-lying states. Starting from the snapshots sampled by these adiabatic trajectories, we performed geometry optimizations to locate the LE and CT minima on the S_1 state.

Fig. S3 illustrates the time evolution of the S_1 state's characters of the 75 post-AIMS adiabatic S_1 trajectories. Both the S_1 dipole moment (in Debye) and the S_0-S_1 energy gaps were analyzed. The evolution of S_1 dipole moments reveals the dynamical stability of the LE and CT minima, consistent with our SS-AIMS results in **Fig. 3B**. Dipole moment values below 20 Debye indicate LE character, and values above 25 Debye indicate CT character. The trajectories exhibiting LE characters generally exhibit larger S_0-S_1 energy gaps compared to those with CT characters (**Fig. S3**). The smallest S_0-S_1 energy gap observed for all trajectories was 0.6 eV in a CT minimum, which was still too large to trigger significant $S_1 \rightarrow S_0$ decay even if the AIMS simulations had been run. This finding also suggests that the $S_1 \rightarrow S_0$ decay is most probably beyond 1 ps timescale, which will not be further investigated in this study. It is noteworthy that except for one trajectory transitioning from LE to CT character, there is no other transition events between

the two characters. Thus, the trajectories largely remain in their S_1 minima of either LE or CT character throughout the post-AIMS adiabatic dynamics.

Multiple S_1-state minima with LE and CT characters were discovered by optimizing the snapshots randomly selected from the S_1 adiabatic trajectories (**Table S1**). Two types of LE minima were observed, one with high S_0-S_1 excitation energies and the other with lower ones (**Table S1**). The CT minima mostly have lower S_0-S_1 excitation energy than both types of LE minima. *Importantly, the LE minimum with the lower excitation energy between 2.5 – 2.8 eV was not previously reported. and is a key finding in this study.* Following the $S_2 \rightarrow S_1$ relaxation, some trajectories quickly reached the LE minimum with the higher excitation energy and were temporarily stabilized there. However, eight trajectories were found to escape this minimum during the 1 ps adiabatic dynamics and reached the LE minimum with lower excitation energy and got stabilized there (**Fig. S4A**). **Fig. S4B** compares the distribution of S_0-S_1 energy gaps of the S_1-state TBFs after the SS-AIMS simulation was completed and after 1 ps subsequent propagation on the S_1 state. It is evident that some trajectories with energy gaps near 3.0 eV at the end of SS-AIMS simulation eventually evolved into low-energy LE minima with energy gaps below 2.8 eV. Taken together, these results imply that the LE minimum with lower excitation energy is energetically lower and thermodynamically more stable than the one with higher excitation energy. As will be discussed below, this low-energy LE minimum can slow down the adiabatic ET event following photoexcitation to a bright S_1 state.

The stability of the CT minima was further examined by initiating 15 adiabatic S_1-state trajectories for another 0.9 ps from the optimized structures of the CT minima, starting with random velocities and propagated in the constant NVT ensemble (**Fig. S5**). These additional simulations further confirm the dynamic stability of the CT minima, because randomly thermalized velocities ensured a statistically

meaningful evaluation by mitigating biases from original ICs. As illustrated in **Fig. S5**, the S_1 dipole moment remains around 30 Debye throughout the simulation, indicating that no CT to LE transitions were observed. Furthermore, the S_0-S_1 gap remains around 1 eV, which agrees with previous results. These findings suggest that the CT state, once formed, remains stable at the picosecond timescale. The dynamical stability of the CT minima is particularly crucial for the function of cryptochromes because it corresponds to the formation of a stable radical pair [$FAD^{\bullet+}$-$W400^{\bullet-}$]. Our results indicate that once the radical pair is formed on the S_1 state through the non-adiabatic pathway, it can be stabilized until further ET steps downstream of the tryptophan chain, which further corroborates the viability of the non-adiabatic ET mechanism.

Adiabatic ET step on the S_1 state

In the 1 ps S_1 state adiabatic dynamics following the SS-AIMS simulation, the transitions between the LE and CT minima were a rare event with less than 2% probability (**Fig. S3**). This implies the existence of energy barriers between these minima. To estimate the magnitude of the barriers, the NEB method was employed to optimize the minimum energy paths (MEPs) connecting the LE and CT minima on the S_1 state at the SA-4-CASSCF(6,6)/6-31G*/MM level of theory in the *At*CRY1 (see Methods). The PESs along the MEPs are displayed in **Fig. 4**. Starting from the low-energy LE minimum, a large energy barrier (>5 kcal/mol) needs to be overcome to reach the high-energy LE minimum (**Fig. 4A**). Starting from the high-energy LE minimum, there is a smaller energy barrier of ~0.6 kcal/mol to be overcome to reach the CT minimum (**Fig. 4B**), and the CT→LE barrier is higher than 5 kcal/mol (**Fig. 4B**). These results confirm our above-mentioned finding that the LE minima with the lower S_0-S_1 gap also have a lower energy on the S_1-state PES. The structures of the FWD complex corresponding to the MEP endpoints and highest images are shown in **Fig. S6**. Notably, the structural similarities among these structures indicate that the

character of the excited states is sensitive to the molecular geometry, particularly at the isoalloxazine ring of the FAD. The excited-state energy barriers separating the LE and CT minima are consistent with the observation that the post-AIMS S_1 adiabatic trajectories exhibit transitions from the high-energy to the low-energy LE minima, and that the CT→LE transition is absent. Also, the results suggested that adiabatic ET events can be slowed down by the low-energy LE minima if the photoexcitation directly populates the bright S_1 state with LE character.

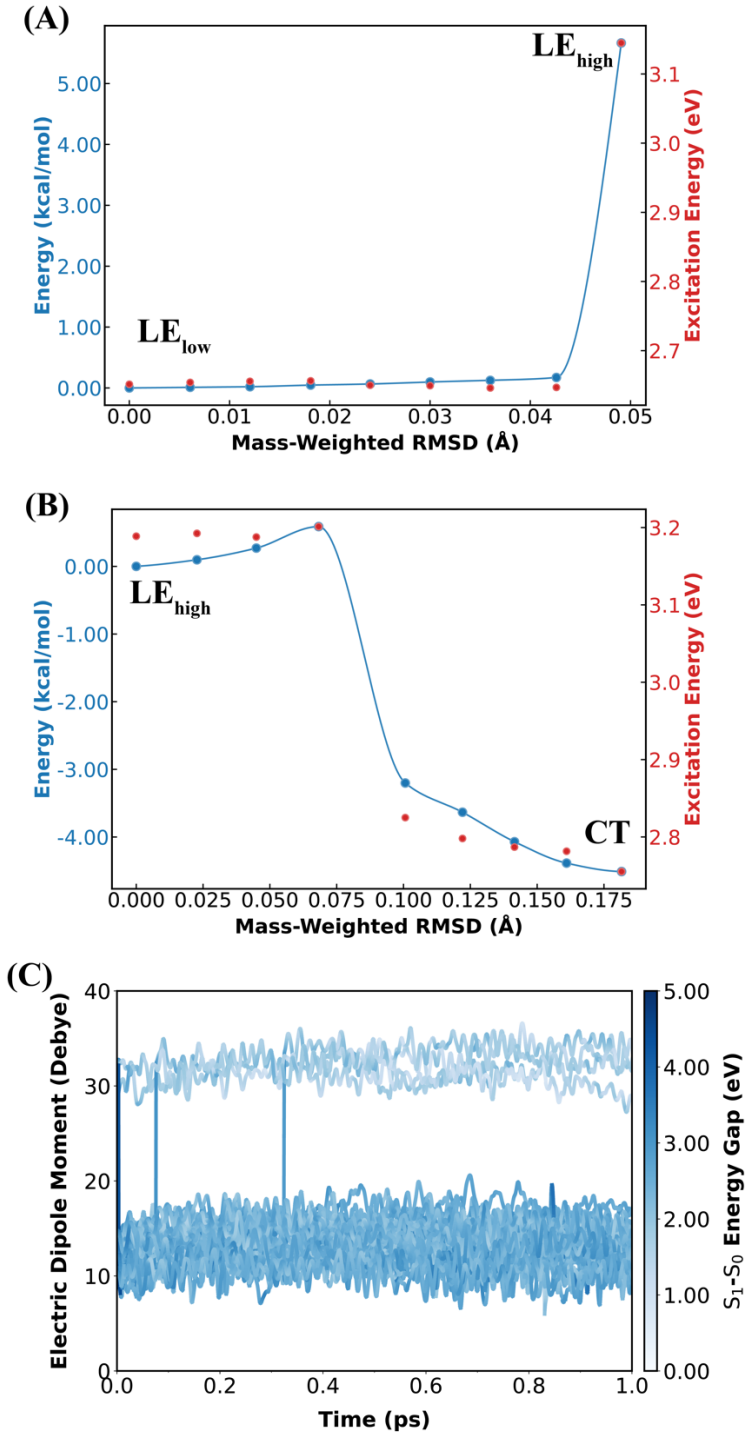

Figure 4. (A) Minimum energy pathways (MEPs) on the S_1 state connecting the low-energy to the high-energy LE minima (labeled as LE_{low} and LE_{high}, respectively). (B) MEP on the S_1 state connecting the high-energy LE minimum to the CT minimum. The MEP are shown as blue curves and dots. The S_1-S_0 energy gaps of each image along the MEP are shown as red dots. The MEPs were optimized using the NEB method at SA-4-CASSCF(6,6)/6-31G*/MM level of theory. (C) Time evolution of the S_1 dipole moment of 50 S_1 adiabatic trajectories starting from the ICs sampled in the FC region featuring a bright

S_1 state with LE character. The adiabatic dynamics were propagated in the constant NVE ensemble. The shade of the color represents the S_1-S_0 energy gap. The majority of the trajectories (~92%) are stabilized in the S_1-state LE minima visited soon after the photoexcitation to the S_1 state. The S_1-S_0 energy gaps oscillate between 0.66 eV and a maximum value of 4.80 eV throughout the simulation. All on-the-fly QM/MM calculations were carried out at SA-4-CASSCF(6,6)/6-31G*/MM level of theory.

To test this hypothesis, we initiated adiabatic S_1-state dynamics from the ICs in the FC region having a bright S_1 state with LE character, which is dominant in the set of all sampled ICs (**Fig. 2**). **Fig. 4C** illustrates the evolution of the S_1 dipole moment of 50 ICs. Only four trajectories (~ 8% of total trajectories) underwent the adiabatic transition from the LE to the CT minima. The lowest S_0-S_1 gap observed among all trajectories is 0.66 eV, which is still sufficiently large to avoid non-adiabatic decay to the S_0 state even if the AIMS simulations had been performed. Taken together, these observations suggest that many S_1 state trajectories are stabilized in the low-energy LE minima which prevents easy access to the CT minima, in agreement with our above-mentioned MEP analysis.

These findings indicate that the initial photoinduced ET can occur adiabatically on the S_1 state following photoexcitation to the S_1 state, resulting in the formation of the radical pair. However, the energy barrier may slow this process. Therefore, the non-adiabatic ET provides an alternative route to complement the adiabatic one, facilitating radical pair formation. Additionally, thermal fluctuations on the ground state are essential for non-adiabatic ET events by means of changing the state order in the FC region.

Influence of the Protein Environment

It is well known that the molecular environment has significant effects in modulating photochemical reactions.[56-65] In proteins, these effects usually arise from the electrostatic potential created by the hydrophilic residues and the steric restrictions in the binding pocket of the chromophore[56-58, 60, 62]. For *At*CRY1, the spatial arrangement of the FAD and the tryptophan triad is particularly important for the successful production of a long-distance separated radical pair through a cascade of ET events since it influences the overlap of molecular orbitals between donors and acceptors. Also, the electrostatics created

by the protein can also play essential roles since it can change the relative stability of LE and CT minima of excited states, as well as the energy barriers connecting them.

To assess the influence of the electrostatics on the characters and relative energies of the S_1 minima, we performed constrained QM/MM optimization on the S_1 state, starting from 63 ICs in the sampled in the post-AIMS S_1-state adiabatic trajectories. Only the active region, i.e., the FWD complex (**Fig. 1B&C**), was allowed to relax, while the rest of the system was fixed. After constrained optimization, the FWD complex was extracted from the protein matrix, and a single-point energy calculation was performed in the vacuum (see SI Method). **Fig. S7** illustrates the distributions of the S_1-S_0 energy gap and the character of the S_1 state calculated in both environments using identical geometries of the FWD complex. It highlights the substantial differences between these two environments. In the protein environment, the S_0-S_1 energy gaps exhibit a bimodal distribution, with peaks at approximately 2.7 eV and 3.1 eV (**Fig. S7A)**. Most of the sampled structures (46 out of 63) have an S_1 state with LE character. Conversely, in the vacuum, the S_0-S_1 energy gap distribution is centered around 2.7 eV but displays a broader spread in the lower-energy range (**Fig. S7B**). This shift correlates with a significant increase in the frequency of the CT character, found in 61 out of 63 geometries, while only two geometries exhibit LE character. The data suggests that protein electrostatics favors local excitation on the FAD. *It is an interesting result since the protein electrostatics usually facilitate the catalyzed reaction, such as in enzymatic catalysis, instead of hindering it.*

Additional new insights were obtained from optimizing the FWD complex in the vacuum on the S_1 state under different conditions: (1) the atoms previously at the QM/MM boundary were fixed to the corresponding positions in the protein, and (2) full relaxation of all atoms. The results are presented in **Figs. 5A&B**. In total, 28 structures were optimized in both conditions. Optimized structures with

positional constraints yielded both LE and CT minima on the S_1 state. In contrast, the fully relaxed optimizations yielded only CT minima. The removal of constraints allows the FAD and W400 to change their relative orientations with respect to each other, thus lowering the energy of the charge transfer minima. The **Figs. 5C&D** presents the structures of FWD optimized under different conditions, comparing the structures in the protein environment and the vacuum, with and without structural constraints from the protein, respectively. Taken together, these results indicate that the protein environment prevents facile adiabatic ET between FAD and W400 by creating more unfavorable electrostatics and steric constraints compared to the vacuum.

The above analysis appears counterintuitive: how can the *At*CRY1 hinder the initial ET step if one of their main functions is to harness light energy to create and propagate radical pairs? The answer to this key question lies in the downstream ET steps following the initial ET from W400 to FAD. The constraints imposed by the protein environment may ensure the correct relative orientation between W400 and its neighboring W377 that maximizes their overlap in molecular orbitals, resulting in optimal diabatic coupling to facilitate the next step of the ET from W400 to W377. **Fig. 5C&D** illustrates how the protein restricts and stabilizes orientations of the FWD complex with respect to the W377, compared to the optimized structures of FDW in the vacuum. Thus, we hypothesize that the protein environment's role is to speed up the subsequent ET steps between the tryptophan residues at the cost of slightly slowing down the first ET step between the FAD and W400. This hypothesis needs to be tested in future work using Marcus's theory in the vacuum and protein environments for subsequent ET steps.

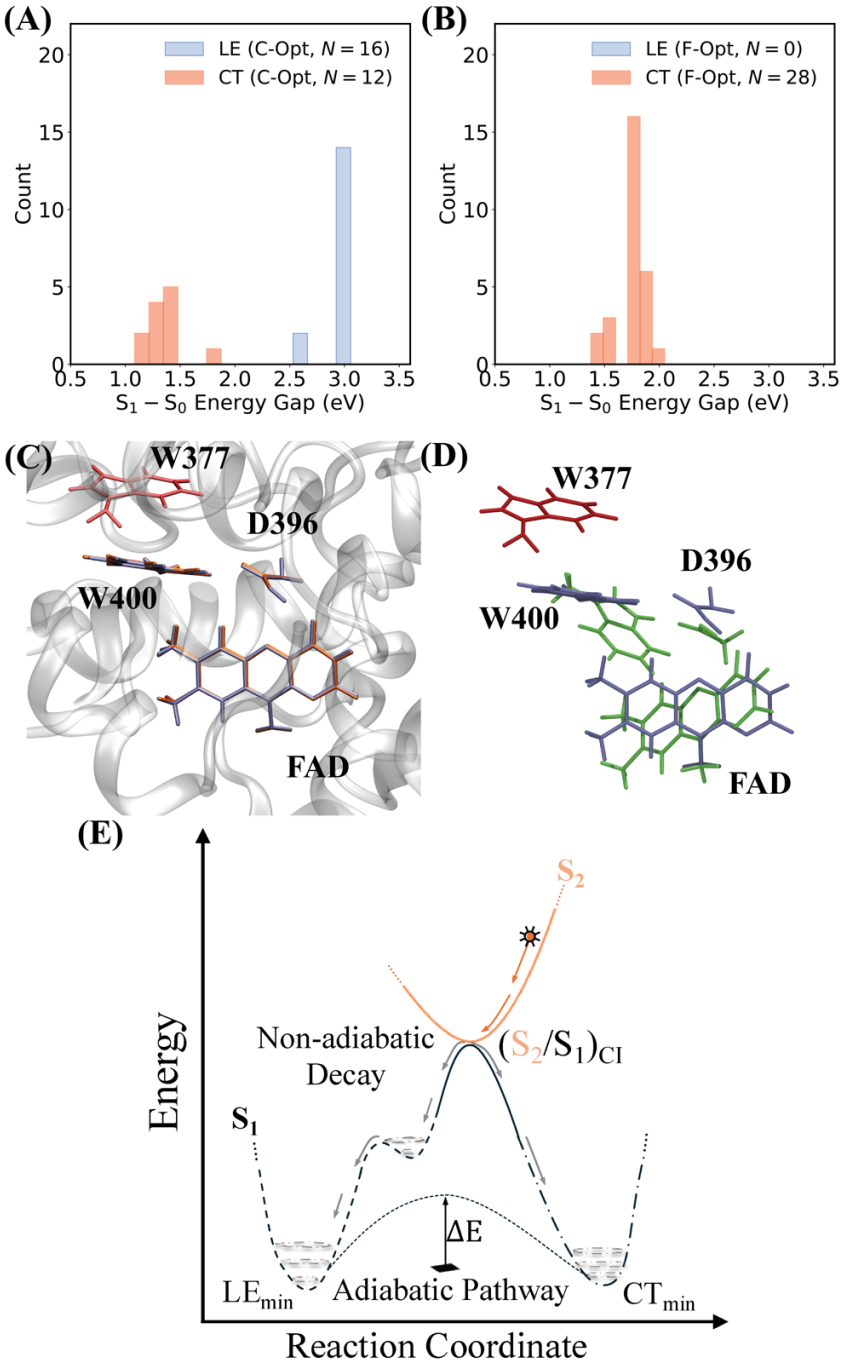

Figure 5. (A) Distributions of S_0-S_1 energy gaps and characters of the S_1 state of the FWD complex after (A) constrained optimization (C-Opt) and (B) free optimization (F-Opt) in the vacuum on the S_1 state at the SA-4-CASSCF(6,6)/6-31G* level of theory. The dataset comprises 28 distinct optimized structures in the vacuum starting from sampled snapshots in the S_1-state adiabatic dynamics in protein. (C) Structural representation of the active region in the *At*CRY1 binding pocket. The S_1-state LE and CT minima are colored in blue and orange, respectively, for the FDW complex. The W377 residue lying downstream in the ET cascade from W400 is colored in red. (D) Comparison between the FWD's structures in the CT

minima optimized in the protein environment (blue) and in the vacuum (green), highlighting the effects of the binding pocket in maintaining the relative orientation between the W400 and W377 residues. The geometries were aligned at the terminal methyl group of the flavin moiety (depicted in **Fig. 1**). (E) Schematic representation of the non-adiabatic and adiabatic ET mechanisms in the *At*CRY1. The non-radiative mechanism mediated via S_2/S_1 CI is depicted at the top, with the orange curve representing the S_2-state PES. The two LE minima on the S_1-state PES are illustrated by the dashed black curve. The dotted-dashed line represents the CT minimum. The adiabatic ET pathway connecting the LE and CT minima is shown as a fine-dotted curve with the adiabatic energy barrier indicated as ΔE.

Discussions and Conclusions

In this work, the mechanism of the initial step of photoinduced ET in *At*CRY1 was systematically characterized by extensive non-adiabatic and adiabatic dynamics simulations with multireference *ab initio* QM/MM calculations. The key new findings are summarized as follows. First, ET from the W400 residue to the FAD can proceed through the ultrafast $S_2 \rightarrow S_1$ nonradiative decay within a few tens of femtoseconds, which is complementary to the slower adiabatic ET on the S_1 state. The non-radiative ET pathway is physically meaningful and relevant due to the noticeable amount of conformations in the FC region that has a bright S_2 state. Its significance also arises from the large portion of the S_1 population dynamically stabilized in the CT minima after the $S_2 \rightarrow S_1$ decay. To the best of our knowledge, this new pathway has not been previously investigated using computational modeling as rigorous as this work.

Second, two types of LE minima on the S_1 state were discovered following the non-adiabatic relaxation, and the low-energy LE minimum can slow down the adiabatic ET. The high-energy LE minimum was previously identified by geometry optimizations at the CASSCF level of theory with a smaller active space than this study[41] without dynamics simulation. It was considered the only LE minimum before reaching the CT minimum in the adiabatic pathway. In this work, however, through extensive S_1-state CASSCF QM/MM adiabatic dynamics with a larger active space, both following the $S_2 \rightarrow S_1$ decay and starting from FC region, we show that the high-energy LE minimum is metastable, and it can quickly relax to the newly identified low-energy LE minimum (**Fig. S4**). It stabilizes the LE character and thus slows down the

adiabatic ET event. This new discovery is significant because it deepens our understanding of the key features of PES on the S_1 state that influence the kinetics of ET.

Third, the CT minima on the S_1 state visited after the non-radiative decay remains dynamically stable on the picosecond timescale. Even with the excess kinetic energy after the decay, the CT minimum is stable enough to prevent backward transitions to the LE minimum, which would have eliminated the newly generated radical pair. Also, the stable CT minima can better prepare the system for the next ET step from the W400 to the W377. Noticeably, during all trajectory dynamics, the S_1 and S_0 states were never close to being degenerate. This suggested that the $S_1 \rightarrow S_0$ decay may take place in a longer timescale. Future studies will be focused on this aspect.

Last but not least, the protein environment does not facilitate the initial ET from the W400 to FAD, if not slowing down this process. The electrostatics and steric restrictions created by the protein stabilize the LE minimum more than the CT minimum on the S_1 state, disfavoring the initial ET event. However, the arrangements of the side chains of the tryptophan residues in the protein could ensure good overlap in the molecular orbitals between them, thus enabling quick subsequent ET steps. Although the initial ET might, in principle, occur more quickly in the absence of the protein environment, the large reorientation of the tryptophan residues without the protein's steric constraints can make subsequent ET difficult. *Thus, the protein environment balances the kinetics of different ET steps to maximize the overall quantum efficiency.* This new interpretation of the role of protein on the ET in cryptochromes deepens our understanding of photoreactions in biomolecules.

In **Fig. 5E,** we schematically summarize our new findings regarding the pathways of non-adiabatic and adiabatic ET in *At*CRY1. In conclusion, through comprehensive and accurate computational characterizations of different reaction pathways, our study complements the existing picture of the ET in light-sensing cryptochromes, deepening the fundamental understanding of the initial ET step in them. Our

findings highlight the intricate interplay among molecular geometry, excited-state characters, and ET dynamics. As such, our study contributes to the broader field of photochemistry and photobiology by elucidating molecular mechanisms that govern light-induced charge transfer events in photoreceptors.

Summary of Computational Methods

Detailed computational methods are provided in the SI.

The system setup was initiated from the crystal structure of *At*CRY1 (PDB code: 1U3C)[66], with missing terminal residues rebuilt using the MODELLER software package[67] and protonation states assigned at neutral pH (D396 was assigned as protonated to favor photoinduced electron transfer[26, 41]) using the H++ server[68]. The protein, along with crystallographic water molecules and Mg^{2+} ions, was solvated in a periodic box, modeled with the Amber ff14SB force field and the SPC/Fw water model[69], while the FAD chromophore was parameterized via GAFF procedure[70, 71] in its fully oxidized, dark-adapted state. Initial classical MD simulations involved restrained energy minimization, gradual heating and relaxation of restraints, followed by a 10 ns production run in the constant NPT ensemble at 300 K temperature and 1 atm pressure.

Subsequently, ground-state QM/MM MD equilibration was performed on 20 configurations sampled from the classical MD trajectory with 0.5 ns time interval in order to refine the equilibrium structures of the FDW complex in the FC region. In these simulations, the QM region (**Fig. 1B&C**) was treated with DFT using the ωPBEh functional[72, 73] and a 6-31G* basis set[74, 75], while the MM region maintained the classical force field description. The QM and MM regions were coupled through electrostatic embedding. For excited-state calculations in the FC region, vertical excitation energies and oscillator strengths were calculated for 300 configurations sampled from ground-state QM/MM MD simulation, using the XMS-CASPT2//SA(4)-CASSCF(6,6)/6-31G*/MM approach[54, 76]. The excited states were assigned as either LE or CT character based on Mulliken charges and dipole moments.

The photoinduced electron transfer process was further examined through non-adiabatic dynamics using the stochastic-selection AIMS (SS-AIMS) method, initiated from selected bright S_2 states to probe $S_2 \rightarrow S_1$ decay starting from 15 ICs. These simulations, conducted with on-the-fly SA-4-CASSCF(6,6)/6-31G*/MM calculations, were extended up to 500 fs and averaged over 5 runs for each IC to capture state populations and charge evolutions. 75 S_1-state adiabatic dynamics simulations were launched, restarting from the coordinates and velocities of S_1 TBF centroids at the end of the SS-AIMS simulation and propagated in the constant NVE ensemble to ensure the continuation of the dynamics from SS-AIMS. Additionally, 15 S_1-state dynamics simulations were launched from the optimized CT minima with random velocity and propagated in the constant NVT at 300K ensemble to test the stability of the CT minima. Furthermore, 50 S_1-state adiabatic dynamics simulations were launched on the S_1 state in the FC region, starting from ICs with bright S_1 state of LE character, in order to simulate the direct dynamics of adiabatic ET following photoexcitation to the S_1 state. Excited-state geometry and reaction pathway optimizations, including constrained geometry optimizations and nudged elastic band calculations, were performed to delineate the energy landscape connecting S_1-state LE and CT minima. Geometry optimizations in the vacuum with and without positional constraints were also carried out to elucidate the protein's effect on the ET mechanism.

All classical MD simulations were executed using the GPU-accelerated version of the AMBER software package (v. 20)[77]. Ground-state QM/MM MD simulations were performed with the TeraChem[78-81] software package interfaced with the OpenMM[82] package. QM/MM calculations of the absorption spectra were performed using the OpenMolcas[83] interfaced with the Tinker software packages.[84] All SS-AIMS were propagated using the FMS90 code interfaced with the TeraChem/OpenMM packages. All excited-state geometry optimizations and MEP optimizations were carried out using the TeraChem package.

Supplemental information

The supplemental information contains the detailed computational method. It also contains Figures S1-S7. They include the active space of the CASSCF method, the characterization of ICs in terms of oscillator strength, the LE/CT character, and S_0-S_1 excitation energies, the analysis of post-AIMS adiabatic trajectories stabilized in the LE and CT minima, the analysis of adiabatic trajectories undergoing transition from LE_{high} to LE_{low} S_1-state minima, the critical points along the MEP on the S_1 state, and the effects of electrostatics on the distribution of LE and CT characters of the S_1 state. In addition, Table S1 illustrates the photophysical properties of the representative structures of the three types of S_1-state minima.

AUTHOR INFORMATION

Corresponding Author

Ruibin Liang

ORCID: 0000-0001-8741-1520

Notes

The authors declare no competing financial interests.

Acknowledgments

This work was supported by the National Institutes of Health Grants R35GM150780. We also acknowledge the computing facilities provided by the High-Performance Computing Center at Texas Tech University.

References

(1) Ahmad, M.; Jarillo, J. A.; Smirnova, O.; Cashmore, A. R. Cryptochrome blue-light photoreceptors of Arabidopsis implicated in phototropism. *Nature* **1998**, *392* (6677), 720-723. DOI: 10.1038/33701.
(2) Cashmore, A. R.; Jarillo, J. A.; Wu, Y.-J.; Liu, D. Cryptochromes: Blue Light Receptors for Plants and Animals. *Science* **1999**, *284* (5415), 760-765. DOI: 10.1126/science.284.5415.760.
(3) Ahmad, M.; Cashmore, A. R. Seeing blue: the discovery of cryptochrome. *Plant Mol. Biol.* **1996**, *30* (5), 851-861. DOI: 10.1007/BF00020798.
(4) Dodson, C. A.; Hore, P. J.; Wallace, M. I. A radical sense of direction: signalling and mechanism in cryptochrome magnetoreception. *Trends Biochem. Sci.* **2013**, *38* (9), 435-446. DOI: https://doi.org/10.1016/j.tibs.2013.07.002.
(5) Sancar, A.; Lindsey-Boltz, L. A.; Kang, T.-H.; Reardon, J. T.; Lee, J. H.; Ozturk, N. Circadian clock control of the cellular response to DNA damage. *FEBS Lett.* **2010**, *584* (12), 2618-2625. DOI: https://doi.org/10.1016/j.febslet.2010.03.017.
(6) Sancar, A. Structure and Function of DNA Photolyase and Cryptochrome Blue-Light Photoreceptors. *Chem. Rev.* **2003**, *103* (6), 2203-2238. DOI: 10.1021/cr0204348.
(7) Lin, C.; Shalitin, D. Cryptochrome Structure and Signal Transduction. *Annu. Rev. Plant Biol.* **2003**, *54* (1), 469-496. DOI: 10.1146/annurev.arplant.54.110901.160901.
(8) Chaves, I.; Pokorny, R.; Byrdin, M.; Hoang, N.; Ritz, T.; Brettel, K.; Essen, L.-O.; van der Horst, G. T. J.; Batschauer, A.; Ahmad, M. The Cryptochromes: Blue Light Photoreceptors in Plants and Animals. *Annu. Rev. Plant Biol.* **2011**, *62* (1), 335-364. DOI: 10.1146/annurev-arplant-042110-103759.
(9) Hore, P. J.; Mouritsen, H. The Radical-Pair Mechanism of Magnetoreception. *Annual Review of Biophysics* **2016**, *45* (1), 299-344. DOI: 10.1146/annurev-biophys-032116-094545.
(10) Hanić, M.; Schuhmann, F.; Frederiksen, A.; Langebrake, C.; Manthey, G.; Liedvogel, M.; Xu, J.; Mouritsen, H.; Solov'yov, I. A. Computational Reconstruction and Analysis of Structural Models of Avian Cryptochrome 4. *J. Phys. Chem. B* **2022**, *126* (25), 4623-4635. DOI: 10.1021/acs.jpcb.2c00878.
(11) Sancar, A. Cryptochrome: The Second Photoactive Pigment in the Eye and Its Role in Circadian Photoreception. *Annu. Rev. Biochem.* **2000**, *69* (1), 31-67. DOI: 10.1146/annurev.biochem.69.1.31.
(12) Lin, C.; Feng, S.; DeOliveira, C. C.; Crane, B. R. Cryptochrome–Timeless structure reveals circadian clock timing mechanisms. *Nature* **2023**, *617* (7959), 194-199. DOI: 10.1038/s41586-023-06009-4.
(13) Smyllie, N. J.; Bagnall, J.; Koch, A. A.; Niranjan, D.; Polidarova, L.; Chesham, J. E.; Chin, J. W.; Partch, C. L.; Loudon, A. S. I.; Hastings, M. H. Cryptochrome proteins regulate the circadian intracellular behavior and localization of PER2 in mouse suprachiasmatic nucleus neurons. *Proc. Natl. Acad. Sci. U. S. A.* **2022**, *119* (4), e2113845119. DOI: 10.1073/pnas.2113845119.
(14) Ahmad, M.; Cashmore, A. R. HY4 gene of A. thaliana encodes a protein with characteristics of a blue-light photoreceptor. *Nature* **1993**, *366* (6451), 162-166. DOI: 10.1038/366162a0.
(15) Guo, H.; Yang, H.; Mockler, T. C.; Lin, C. Regulation of Flowering Time by Arabidopsis Photoreceptors. *Science* **1998**, *279* (5355), 1360-1363. DOI: 10.1126/science.279.5355.1360.
(16) Solov'yov, I. A.; Ritz, T.; Schulten, K.; Hore, P. J. A chemical compass for bird navigation. In *Quantum Effects in Biology*, Mohseni, M., Omar, Y., Engel, G. S., Plenio, M. B. Eds.; Cambridge University Press, 2014; pp 218-236.
(17) Ritz, T.; Adem, S.; Schulten, K. A Model for Photoreceptor-Based Magnetoreception in Birds. *Biophys. J.* **2000**, *78* (2), 707-718. DOI: https://doi.org/10.1016/S0006-3495(00)76629-X.

(18) Solov'yov, I. A.; Mouritsen, H.; Schulten, K. Acuity of a Cryptochrome and Vision-Based Magnetoreception System in Birds. *Biophys. J.* **2010**, *99* (1), 40-49. DOI: https://doi.org/10.1016/j.bpj.2010.03.053.
(19) Xu, J.; Jarocha, L. E.; Zollitsch, T.; Konowalczyk, M.; Henbest, K. B.; Richert, S.; Golesworthy, M. J.; Schmidt, J.; Déjean, V.; Sowood, D. J. C.; et al. Magnetic sensitivity of cryptochrome 4 from a migratory songbird. *Nature* **2021**, *594* (7864), 535-540. DOI: 10.1038/s41586-021-03618-9.
(20) Kar, R. K.; Miller, A.-F.; Mroginski, M.-A. Understanding flavin electronic structure and spectra. *WIREs Computational Molecular Science* **2022**, *12* (2), e1541. DOI: https://doi.org/10.1002/wcms.1541.
(21) Liu, B.; Liu, H.; Zhong, D.; Lin, C. Searching for a photocycle of the cryptochrome photoreceptors. *Curr. Opin. Plant Biol.* **2010**, *13* (5), 578-586. DOI: https://doi.org/10.1016/j.pbi.2010.09.005.
(22) Karki, N.; Vergish, S.; Zoltowski, B. D. Cryptochromes: Photochemical and structural insight into magnetoreception. *Protein Sci.* **2021**, *30* (8), 1521-1534.
(23) Schwinn, K.; Ferré, N.; Huix-Rotllant, M. UV-visible absorption spectrum of FAD and its reduced forms embedded in a cryptochrome protein. *Phys. Chem. Chem. Phys.* **2020**, *22* (22), 12447-12455, 10.1039/D0CP01714K. DOI: 10.1039/D0CP01714K.
(24) Müller, P.; Bouly, J.-P.; Hitomi, K.; Balland, V.; Getzoff, E. D.; Ritz, T.; Brettel, K. ATP Binding Turns Plant Cryptochrome Into an Efficient Natural Photoswitch. *Sci. Rep.* **2014**, *4* (1), 5175. DOI: 10.1038/srep05175.
(25) Timmer, D.; Frederiksen, A.; Lünemann, D. C.; Thomas, A. R.; Xu, J.; Bartölke, R.; Schmidt, J.; Kubař, T.; De Sio, A.; Solov'yov, I. A.; et al. Tracking the Electron Transfer Cascade in European Robin Cryptochrome 4 Mutants. *J. Am. Chem. Soc.* **2023**, *145* (21), 11566-11578. DOI: 10.1021/jacs.3c00442.
(26) Cailliez, F.; Müller, P.; Gallois, M.; de la Lande, A. ATP Binding and Aspartate Protonation Enhance Photoinduced Electron Transfer in Plant Cryptochrome. *J. Am. Chem. Soc.* **2014**, *136* (37), 12974-12986. DOI: 10.1021/ja506084f.
(27) Lüdemann, G.; Solov'yov, I. A.; Kubař, T.; Elstner, M. Solvent Driving Force Ensures Fast Formation of a Persistent and Well-Separated Radical Pair in Plant Cryptochrome. *J. Am. Chem. Soc.* **2015**, *137* (3), 1147-1156. DOI: 10.1021/ja510550g.
(28) Firmino, T.; Mangaud, E.; Cailliez, F.; Devolder, A.; Mendive-Tapia, D.; Gatti, F.; Meier, C.; Desouter-Lecomte, M.; de la Lande, A. Quantum effects in ultrafast electron transfers within cryptochromes. *Phys. Chem. Chem. Phys.* **2016**, *18* (31), 21442-21457, 10.1039/C6CP02809H. DOI: 10.1039/C6CP02809H.
(29) Mendive-Tapia, D.; Mangaud, E.; Firmino, T.; de la Lande, A.; Desouter-Lecomte, M.; Meyer, H.-D.; Gatti, F. Multidimensional Quantum Mechanical Modeling of Electron Transfer and Electronic Coherence in Plant Cryptochromes: The Role of Initial Bath Conditions. *J. Phys. Chem. B* **2018**, *122* (1), 126-136. DOI: 10.1021/acs.jpcb.7b10412.
(30) Sjulstok, E.; Lüdemann, G.; Kubař, T.; Elstner, M.; Solov'yov, I. A. Molecular Insights into Variable Electron Transfer in Amphibian Cryptochrome. *Biophys. J.* **2018**, *114* (11), 2563-2572. DOI: 10.1016/j.bpj.2018.04.014.
(31) Lacombat, F.; Espagne, A.; Dozova, N.; Plaza, P.; Müller, P.; Brettel, K.; Franz-Badur, S.; Essen, L.-O. Ultrafast Oxidation of a Tyrosine by Proton-Coupled Electron Transfer Promotes Light Activation of an Animal-like Cryptochrome. *J. Am. Chem. Soc.* **2019**, *141* (34), 13394-13409. DOI: 10.1021/jacs.9b03680.
(32) Zoltowski Brian, D.; Chelliah, Y.; Wickramaratne, A.; Jarocha, L.; Karki, N.; Xu, W.; Mouritsen, H.; Hore Peter, J.; Hibbs Ryan, E.; Green Carla, B.; et al. Chemical and structural analysis of a photoactive vertebrate cryptochrome from pigeon. *Proc. Natl. Acad. Sci. U. S. A.* **2019**, *116* (39), 19449-19457. DOI: 10.1073/pnas.1907875116.

(33) Wang, Y.; Veglia, G.; Zhong, D.; Gao, J. Activation mechanism of Drosophila cryptochrome through an allosteric switch. *Science Advances 7* (25), eabg3815. DOI: 10.1126/sciadv.abg3815.
(34) Hanić, M.; Schuhmann, F.; Frederiksen, A.; Langebrake, C.; Manthey, G.; Liedvogel, M.; Xu, J.; Mouritsen, H.; Solov'yov, I. A. Computational Reconstruction and Analysis of Structural Models of Avian Cryptochrome 4. *J. Phys. Chem. B* **2022**. DOI: 10.1021/acs.jpcb.2c00878.
(35) Schuhmann, F.; Kattnig, D. R.; Solov'yov, I. A. Exploring Post-activation Conformational Changes in Pigeon Cryptochrome 4. *J. Phys. Chem. B* **2021**, *125* (34), 9652-9659. DOI: 10.1021/acs.jpcb.1c02795.
(36) Cailliez, F.; Müller, P.; Firmino, T.; Pernot, P.; de la Lande, A. Energetics of Photoinduced Charge Migration within the Tryptophan Tetrad of an Animal (6–4) Photolyase. *J. Am. Chem. Soc.* **2016**, *138* (6), 1904-1915. DOI: 10.1021/jacs.5b10938.
(37) Immeln, D.; Weigel, A.; Kottke, T.; Pérez Lustres, J. L. Primary Events in the Blue Light Sensor Plant Cryptochrome: Intraprotein Electron and Proton Transfer Revealed by Femtosecond Spectroscopy. *J. Am. Chem. Soc.* **2012**, *134* (30), 12536-12546. DOI: 10.1021/ja302121z.
(38) Marcus, R. A. On the Theory of Oxidation - Reduction Reactions Involving Electron Transfer. I. *J. Chem. Phys.* **1956**, *24* (5), 966-978. DOI: 10.1063/1.1742723.
(39) Marcus, R. A. On the Theory of Oxidation - Reduction Reactions Involving Electron Transfer. II. Applications to Data on the Rates of Isotopic Exchange Reactions. *J. Chem. Phys.* **1957**, *26* (4), 867-871. DOI: 10.1063/1.1743423.
(40) Marcus, R. A. On the Theory of Oxidation - Reduction Reactions Involving Electron Transfer. III. Applications to Data on the Rates of Organic Redox Reactions. *J. Chem. Phys.* **1957**, *26* (4), 872-877. DOI: 10.1063/1.1743424.
(41) Solov'yov, I. A.; Domratcheva, T.; Moughal Shahi, A. R.; Schulten, K. Decrypting Cryptochrome: Revealing the Molecular Identity of the Photoactivation Reaction. *J. Am. Chem. Soc.* **2012**, *134* (43), 18046-18052. DOI: 10.1021/ja3074819.
(42) Blumberger, J. Recent Advances in the Theory and Molecular Simulation of Biological Electron Transfer Reactions. *Chem. Rev.* **2015**, *115* (20), 11191-11238. DOI: 10.1021/acs.chemrev.5b00298.
(43) Kretchmer, J. S.; Boekelheide, N.; Warren, J. J.; Winkler, J. R.; Gray, H. B.; Miller, T. F. Fluctuating hydrogen-bond networks govern anomalous electron transfer kinetics in a blue copper protein. *Proc. Natl. Acad. Sci. U. S. A.* **2018**, *115* (24), 6129. DOI: 10.1073/pnas.1805719115.
(44) Matyushov, D. V. Protein electron transfer: Dynamics and statistics. *J. Chem. Phys.* **2013**, *139* (2), 025102. DOI: 10.1063/1.4812788.
(45) Matyushov, D. V. Energetics of Electron-Transfer Reactions in Soft Condensed Media. *Acc. Chem. Res.* **2007**, *40* (4), 294-301. DOI: 10.1021/ar7000167.
(46) LeBard, D. N.; Matyushov, D. V. Protein–water electrostatics and principles of bioenergetics. *Phys. Chem. Chem. Phys.* **2010**, *12* (47), 15335-15348, 10.1039/C0CP01004A. DOI: 10.1039/C0CP01004A.
(47) Kubař, T.; Elstner, M. A hybrid approach to simulation of electron transfer in complex molecular systems. *Journal of The Royal Society Interface* **2013**, *10* (87), 20130415. DOI: 10.1098/rsif.2013.0415.
(48) Nielsen, C.; Nørby, M. S.; Kongsted, J.; Solov'yov, I. A. Absorption Spectra of FAD Embedded in Cryptochromes. *J. Phys. Chem. Lett.* **2018**, *9* (13), 3618-3623. DOI: 10.1021/acs.jpclett.8b01528.
(49) Ben-Nun, M.; Quenneville, J.; Martínez, T. J. Ab Initio Multiple Spawning: Photochemistry from First Principles Quantum Molecular Dynamics. *J. Phys. Chem. A* **2000**, *104* (22), 5161-5175. DOI: 10.1021/jp994174i.
(50) Ben-Nun, M.; Martínez, T. J. Ab Initio Quantum Molecular Dynamics. In *Advances in Chemical Physics*, John Wiley & Sons, Inc., 2002; pp 439-512.
(51) Curchod, B. F. E.; Martínez, T. J. Ab Initio Nonadiabatic Quantum Molecular Dynamics. *Chem. Rev.* **2018**, *118* (7), 3305-3336. DOI: 10.1021/acs.chemrev.7b00423.

(52) Curchod, B. F. E.; Glover, W. J.; Martínez, T. J. SSAIMS—Stochastic-Selection Ab Initio Multiple Spawning for Efficient Nonadiabatic Molecular Dynamics. *J. Phys. Chem. A* **2020**, *124* (30), 6133-6143. DOI: 10.1021/acs.jpca.0c04113.
(53) Siegbahn, P. E. M.; Almlöf, J.; Heiberg, A.; Roos, B. O. The complete active space SCF (CASSCF) method in a Newton–Raphson formulation with application to the HNO molecule. *J. Chem. Phys.* **1981**, *74* (4), 2384-2396. DOI: 10.1063/1.441359.
(54) Shiozaki, T.; Győrffy, W.; Celani, P.; Werner, H.-J. Communication: Extended multi-state complete active space second-order perturbation theory: Energy and nuclear gradients. *J. Chem. Phys.* **2011**, *135* (8), 081106. DOI: 10.1063/1.3633329.
(55) Frederiksen, A.; Gerhards, L.; Reinholdt, P.; Kongsted, J.; Solov'yov, I. A. Importance of Polarizable Embedding for Absorption Spectrum Calculations of Arabidopsis thaliana Cryptochrome 1. *J. Phys. Chem. B* **2024**, *128* (26), 6283-6290. DOI: 10.1021/acs.jpcb.4c02168.
(56) Liang, R.; Bakhtiiari, A. Multiscale simulation unravels the light-regulated reversible inhibition of dihydrofolate reductase by phototrexate. *J. Chem. Phys.* **2022**, *156* (24), 245102. DOI: 10.1063/5.0096349.
(57) Liang, R.; Bakhtiiari, A. Effects of Enzyme–Ligand Interactions on the Photoisomerization of a Light-Regulated Chemotherapeutic Drug. *J. Phys. Chem. B* **2022**, *126* (12), 2382-2393. DOI: 10.1021/acs.jpcb.1c10819.
(58) Bakhtiiari, A.; Costa, G. J.; Liang, R. On the Simulation of Thermal Isomerization of Molecular Photoswitches in Biological Systems. *J. Chem. Theory Comput.* **2023**, *19* (18), 6484-6499. DOI: 10.1021/acs.jctc.3c00451.
(59) Bakhtiiari, A.; Liang, R. Unraveling solvent and substituent effects in the photodynamics of light-dependent microtubule inhibitors for cancer phototherapy. *ChemRxiv* **2024**. DOI: 10.26434/chemrxiv-2024-f48g2.
(60) Liang, R.; Yu, J. K.; Meisner, J.; Liu, F.; Martinez, T. J. Electrostatic Control of Photoisomerization in Channelrhodopsin 2. *J. Am. Chem. Soc.* **2021**, *143* (14), 5425-5437. DOI: 10.1021/jacs.1c00058.
(61) Liang, R.; Liu, F.; Martínez, T. J. Nonadiabatic Photodynamics of Retinal Protonated Schiff Base in Channelrhodopsin 2. *J. Phys. Chem. Lett.* **2019**, *10* (11), 2862-2868. DOI: 10.1021/acs.jpclett.9b00701.
(62) Liang, R.; Das, D.; Bakhtiiari, A. Protein confinement fine-tunes aggregation-induced emission in human serum albumin. *Phys. Chem. Chem. Phys.* **2021**, *23* (46), 26263-26272, 10.1039/D1CP04577F. DOI: 10.1039/D1CP04577F.
(63) Yu, J. K.; Liang, R.; Liu, F.; Martínez, T. J. First-Principles Characterization of the Elusive I Fluorescent State and the Structural Evolution of Retinal Protonated Schiff Base in Bacteriorhodopsin. *J. Am. Chem. Soc.* **2019**, *141* (45), 18193-18203. DOI: 10.1021/jacs.9b08941.
(64) Punwong, C.; Hannongbua, S.; Martínez, T. J. Electrostatic Influence on Photoisomerization in Bacteriorhodopsin and Halorhodopsin. *J. Phys. Chem. B* **2019**, *123* (23), 4850-4857. DOI: 10.1021/acs.jpcb.9b01837.
(65) Liang, R. First-Principles Nonadiabatic Dynamics Simulation of Azobenzene Photodynamics in Solutions. *J. Chem. Theory Comput.* **2021**, *17* (5), 3019-3030. DOI: 10.1021/acs.jctc.1c00105.
(66) Brautigam, C. A.; Smith, B. S.; Ma, Z.; Palnitkar, M.; Tomchick, D. R.; Machius, M.; Deisenhofer, J. Structure of the photolyase-like domain of cryptochrome 1 from Arabidopsis thaliana. *Proc. Natl. Acad. Sci. U. S. A.* **2004**, *101* (33), 12142-12147. DOI: 10.1073/pnas.0404851101.
(67) Webb, B.; Sali, A. Comparative Protein Structure Modeling Using MODELLER. *Curr. Protoc. Bioinform.* **2016**, *54* (1), 5.6.1-5.6.37, https://doi.org/10.1002/cpbi.3. DOI: https://doi.org/10.1002/cpbi.3.

(68) Anandakrishnan, R.; Aguilar, B.; Onufriev, A. V. H++ 3.0: automating p K prediction and the preparation of biomolecular structures for atomistic molecular modeling and simulations. *Nucleic Acids Res.* **2012**, *40* (W1), W537-W541.
(69) Wu, Y.; Tepper, H. L.; Voth, G. A. Flexible simple point-charge water model with improved liquid-state properties. *J Chem Phys* **2006**, *124* (2), 024503. DOI: 10.1063/1.2136877. From NLM Medline.
(70) Wang, J.; Wolf, R. M.; Caldwell, J. W.; Kollman, P. A.; Case, D. A. Development and testing of a general amber force field. *J. Comput. Chem.* **2004**, *25* (9), 1157-1174. DOI: 10.1002/jcc.20035.
(71) Wang, J.; Wang, W.; Kollman, P. A.; Case, D. A. Automatic atom type and bond type perception in molecular mechanical calculations. *J. Mol. Graph. Model.* **2006**, *25* (2), 247-260. DOI: https://doi.org/10.1016/j.jmgm.2005.12.005.
(72) Henderson, T. M.; Izmaylov, A. F.; Scalmani, G.; Scuseria, G. E. Can short-range hybrids describe long-range-dependent properties? *J. Chem. Phys.* **2009**, *131* (4), 044108. DOI: 10.1063/1.3185673.
(73) Rohrdanz, M. A.; Martins, K. M.; Herbert, J. M. A long-range-corrected density functional that performs well for both ground-state properties and time-dependent density functional theory excitation energies, including charge-transfer excited states. *J. Chem. Phys.* **2009**, *130* (5), 054112. DOI: 10.1063/1.3073302.
(74) Hariharan, P. C.; Pople, J. A. The influence of polarization functions on molecular orbital hydrogenation energies. *Theoretica chimica acta* **1973**, *28* (3), 213-222. DOI: 10.1007/BF00533485.
(75) Ditchfield, R.; Hehre, W. J.; Pople, J. A. Self‐Consistent Molecular‐Orbital Methods. IX. An Extended Gaussian‐Type Basis for Molecular‐Orbital Studies of Organic Molecules. *J. Chem. Phys.* **2003**, *54* (2), 724-728. DOI: 10.1063/1.1674902.
(76) Kabir, M. P.; Ghosh, P.; Gozem, S. Electronic structure methods for simulating flavin's spectroscopy and photophysics: comparison of multi-reference, TD-DFT, and single-reference wave function methods. *J. Phys. Chem. B* **2024**, *128* (31), 7545-7557.
(77) Case, D. A.; Belfon, K.; Ben-Shalom, I. Y.; Brozell, S. R.; Cerutti, D. S.; Cheatham, T. E., III; Cruzeiro, V. W. D.; Darden, T. A.; Duke, R. E.; Giambasu, G.; et al. *AMBER 2020*; University of California, San Francisco, 2020.
(78) Ufimtsev, I. S.; Martinez, T. J. Quantum Chemistry on Graphical Processing Units. 3. Analytical Energy Gradients, Geometry Optimization, and First Principles Molecular Dynamics. *J. Chem. Theory Comput.* **2009**, *5* (10), 2619-2628. DOI: 10.1021/ct9003004.
(79) Titov, A. V.; Ufimtsev, I. S.; Luehr, N.; Martinez, T. J. Generating Efficient Quantum Chemistry Codes for Novel Architectures. *J. Chem. Theory Comput.* **2013**, *9* (1), 213-221. DOI: 10.1021/ct300321a.
(80) Seritan, S.; Bannwarth, C.; Fales, B. S.; Hohenstein, E. G.; Kokkila-Schumacher, S. I. L.; Luehr, N.; Snyder, J. W., Jr.; Song, C.; Titov, A. V.; Ufimtsev, I. S.; et al. TeraChem: Accelerating electronic structure and ab initio molecular dynamics with graphical processing units. *J. Chem. Phys.* **2020**, *152* (22), 224110. DOI: 10.1063/5.0007615.
(81) Seritan, S.; Bannwarth, C.; Fales, B. S.; Hohenstein, E. G.; Isborn, C. M.; Kokkila-Schumacher, S. I. L.; Li, X.; Liu, F.; Luehr, N.; Snyder Jr, J. W.; et al. TeraChem: A graphical processing unit-accelerated electronic structure package for large-scale ab initio molecular dynamics. *WIREs Computational Molecular Science* **2021**, *11* (2), e1494. DOI: https://doi.org/10.1002/wcms.1494.
(82) Eastman, P.; Friedrichs, M. S.; Chodera, J. D.; Radmer, R. J.; Bruns, C. M.; Ku, J. P.; Beauchamp, K. A.; Lane, T. J.; Wang, L.-P.; Shukla, D.; et al. OpenMM 4: A Reusable, Extensible, Hardware Independent Library for High Performance Molecular Simulation. *J. Chem. Theory Comput.* **2013**, *9* (1), 461-469. DOI: 10.1021/ct300857j.

(83) Fdez. Galván, I.; Vacher, M.; Alavi, A.; Angeli, C.; Aquilante, F.; Autschbach, J.; Bao, J. J.; Bokarev, S. I.; Bogdanov, N. A.; Carlson, R. K.; et al. OpenMolcas: From Source Code to Insight. *J. Chem. Theory Comput.* **2019**, *15* (11), 5925-5964. DOI: 10.1021/acs.jctc.9b00532.
(84) Rackers, J. A.; Wang, Z.; Lu, C.; Laury, M. L.; Lagardère, L.; Schnieders, M. J.; Piquemal, J.-P.; Ren, P.; Ponder, J. W. Tinker 8: Software Tools for Molecular Design. *J. Chem. Theory Comput.* **2018**, *14* (10), 5273-5289. DOI: 10.1021/acs.jctc.8b00529.